Title "Deformation and failure modelling of high strength adhesives for crash simulation"
To be submitted for "International Journal of Fracture"

Authors: L. Greve[a,*], F. Andrieux[b]
a) Volkswagen AG, 38436 Wolfsburg, Germany,
b) Fraunhofer Institut für Werkstoffmechanik, Woehlerstr. 11, 79108 Freiburg, Germany
*) Corresponding author: tel. +49 (0)5361 9 46562, fax: +49 (0)5361 9 31549, email: lars.greve@volkswagen.de

Abstract
The deformation and failure mechanisms of toughened high strength adhesives used in the automotive industry are very complex and require advanced numerical models for crashworthiness simulation. The theoretical background of two new modelling approaches for thin adhesive layers is presented: firstly, a simplified elastic damaging node-to-element tied interface model approach for convenient and efficient modelling, and secondly a detailed modelling approach for improved accuracy using an elasto-viscoplastic solid element representation of the adhesive layer. The material model parameters required for both approaches are determined by a comprehensive set of experiments, including quasi-static and dynamic adhesive coupon testing, fracture toughness testing, and quasi-static tension/shear (and combined) testing of thin adhesive layers. A more complex adhesively joined assembly of two aluminium extrusions subjected to quasi-static and dynamic loading serves as the final validation example for both modelling approaches. A good agreement of experiments and numerical predictions could be observed for both modelling approaches.

Keywords: yield, plasticity, failure, modelling, crash

Nomenclature

Symbol	Explanation
G_{IC}, G_{IIC}	Critical strain energy release rate for Mode I and Mode II loading
δ_I, δ_{II}	Relative out-of-plane (Mode I) and in-plane (Mode II) interface element displacements
σ_I, σ_{II}	Out-of-plane (Mode I) and in-plane (Mode II) interface element stresses
E, G	Young's modulus, shear modulus
dA, dW	Infinitesimal area and energy
d_I, d_{II}	Out-of-plane (Mode I) and in-plane (Mode II) damage functions
$\langle x \rangle_+$	Operator returns 'x' if $x > 0$ and 0 otherwise
$\sup_{t \le \tau}(x)$	Supremum of x: Maximum of x within the range $0 \le t \le \tau$
I_1, J_2	First invariant of the stress tensor and second invariant of the stress deviator
σ_m	Hydrostatic stress
σ_e	Equivalent von Mises stress
$\mathbf{I}$	Identity matrix
$\boldsymbol{\sigma}$, $\boldsymbol{\varepsilon}^e$, $\boldsymbol{\varepsilon}^p$	Stress tensor, elastic and plastic strain tensor
$\mathbf{E}$	Elasticity matrix
σ_x, τ_{xy}	Axial stress and torque shear stress
$\sigma_T\left(\varepsilon_T^p\right)$	Tensile strain hardening curve
Φ	Yield function
α, β	Shape parameters for the yield function and the flow potential
σ_0	Shift stress value representing the centre of the yield locus
$\tilde{\sigma}$	Effective equivalent stress

C	Fitting parameter for the strain rate model
$\dot{\lambda}$	Plastic multiplier

Abbreviation	Explanation
DCB	Double Cantilever Beam
DF	Deshpande and Fleck
DYN	Dynamic
Exp, Sim	Experiment and Simulation
FE	Finite Element
JC	Johnson and Cook
QS	Quasi-static

1. Introduction

Since bonding utilising thin adhesive layers can significantly improve the bending, torque, and dynamic stiffness in comparison to conventional spot welds, the amount of adhesively joined components in modern vehicle body structures is continuously increasing, e.g. [1]. Of particular interest are toughened high strength epoxy adhesives [2], which offer high strength in conjunction with increased ductility for improved crashworthiness. The ductility limit of these adhesive materials must be known to ensure structural integration of a vehicle during a crash.

Today, vehicle design is significantly supported by virtual prototyping, including numerical crashworthiness analysis using crash simulation codes. Prediction of the complex deformation and failure mechanisms of high strength adhesives requires novel material models and modelling techniques, which must cover the following phenomena:

a) Hydrostatic stress dependent yield. Simple von Mises [3] deviatoric stress theory (J_2 plasticity) does not apply.
b) Material deformation without conservation of the volume.
c) Non-symmetric yield. The compressive yield stress is significantly higher than the tensile yield stress.
d) Strain rate dependent yield and hardening.
e) Hydrostatic stress dependent fracture.
f) Strain rate dependent fracture.

The von Mises yield criterion [3] is based on the assumption that material yield solely depends on deviatoric stresses, $\boldsymbol{\sigma}'_{ij}$. It has been particularly useful for predicting yield of various isotropic metals, where the yield condition is determined by the second invariant J_2 of the deviatoric stress tensor, $\phi_{vonMises} = f\left(J_2\left(\boldsymbol{\sigma}'_{ij}\right)\right)$. However, the yield stress of the high strength epoxy adhesive investigated in this paper also depends on the hydrostatic stress σ_m, which is related to the first invariant of the stress tensor I_1, $\phi_{Adhesive} = f\left(I_1, J_2\right)$. Schlimmer [4] proposed such a hydrostatic stress dependent plasticity model suitable for adhesives, which generalises the yield criteria of Drucker and Prager [5], and by von Mises [3]. The model covers the features (a) and (b) outlined above. Recently, Mahnken [6] has implemented the model in a commercial code for the simulation of elasto-plastic deformation of high strength adhesives subjected to tensile, shear, and combined tensile/shear loading.

A similar plasticity model has been proposed by Deshpande and Fleck (DF) [7] for modelling the deformation of compressible foams, which addresses features (a) and (b) as well. Due to its

simplicity, the DF model is used as the foundation of the plasticity model and is extended in this paper to meet the requirements for adhesive materials by addressing features (c) and (d).

The fracture model by Johnson and Cook (JC) [8] has been successfully applied to predict the plastic failure strain of isotropic metals. The model is based on the principle of accumulated damage, where the rate of damage can depend on the stress triaxiality σ_m/σ_{eq} and also on the strain rate. In this paper the JC model is adopted to predict adhesive failure since it allows modelling features (e) and theoretically also (f) outlined above. It operates in conjunction with the enhanced DF model in order to provide a comprehensive 3D (solid element) material model for high strength adhesives.

Accurate experimental measurement of the failure strains of thin adhesive layers still remains an unresolved issue, since conventional test methods can not be applied. Literature resources concerning dynamic testing provide only information about the dynamic strength of high strength adhesives [9]. An ongoing research project is dedicated to accurate dynamic strain measurement [10] in order to resolve this discrepancy. Due to these current experimental limitations the effect of strain rate dependent failure is not investigated in this paper.

Large scale Finite Element (FE) models used in the automotive industry encourage simple and efficient modelling. Representing adhesive layers using solid elements, as proposed above, obviously leads to increased modelling efforts. Specialised interface elements have been established in the past for tying two separated components. Various different tying methods have been developed, ranging from discontinuous point connections to continuous line or area connections. A valuable summary of references is given in [11].

The main purpose of the interface models was to predict delamination of quasi-brittle laminated composites. Simple quadratic stress failure criteria, e.g. [12], or more advanced criteria based on the critical strain energy release rate ([13], [14]) have been utilised.

More recently, “pseudo-solid” interface elements, using elasto-plastic constitutive laws, have been applied to model adhesive deformation and failure [6]. However, this interface approach uses 4Node-To-4Node connection elements [15], which requires congruent meshes of the bonded components and increases the modelling effort. To overcome these limitations the mesh independent Node-To-Element tied interface provided by the explicit crash code PAM-CRASH^{TM} [16] is used in this paper as an alternative to the solid element modelling approach. The interface approach benefits from available automatic partner search and connection procedures for joining parts, and from a significantly reduced set of material model parameters. The major drawback of the interface approach is the negligence of visco-plastic deformation. Showing the influence of this simplification in comparison with the detailed solid element modelling technique for the predictability of adhesive failure of practical complex structures is another goal in the present study.

2. Theory of material modelling

2.1. The simplified modelling approach (Interface modelling)

The tied connection interface material model (type 303) in PAM-CRASH^{TM} [16] uses an elastic damaging material model. Although the investigated high strength adhesive exhibits considerable plastic deformation, the total displacement prior to failure is very small. Considering pure shear loading of a 0.5mm thick adhesive layer the shear failure strain will be about 80%, which however corresponds to a total shear displacement of only 0.4mm prior to failure. The maximum

displacements are even lower under tensile or combined loading. Based on these considerations plastic deformation in the adhesive interface model is neglected for the interface model, which is not the case for the advanced solid element approach discussed in the next section.

For the interface model the adhesive layer is represented by a series of discontinuous connections of slave nodes and master elements, Figure 1, which can have different mesh topologies. The relative movement of the slave node is decomposed into out-of-plane (Mode I) and in plane shear (Mode II) displacements.

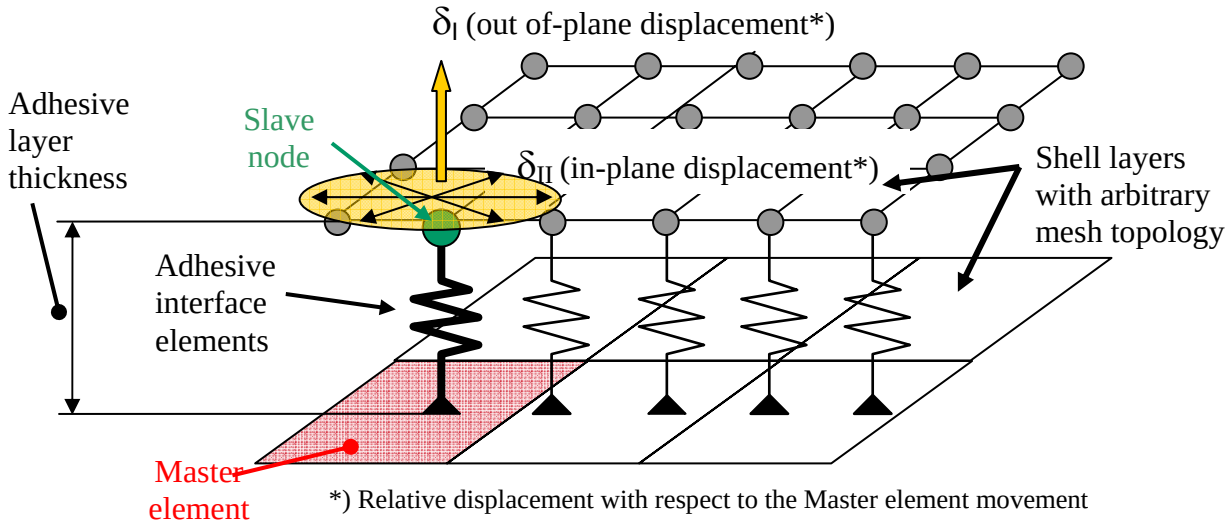

Figure 1. Slave node to Master element connection technique and displacement decomposition of the tied interface material model (type 303) provided in PAMCRASH™.

2.1.1. The critical strain energy release rate

The critical strain energy release rate G_{iC} represents the heart of the interface model. For Mode I loading, the link of this Fracture Mechanics criterion and the corresponding Damage Mechanics formulation used for the interface elements, is shown in Figure 2. The Damage Mechanics law is based on the work by Hillerborg, Modeer and Petersson [17].

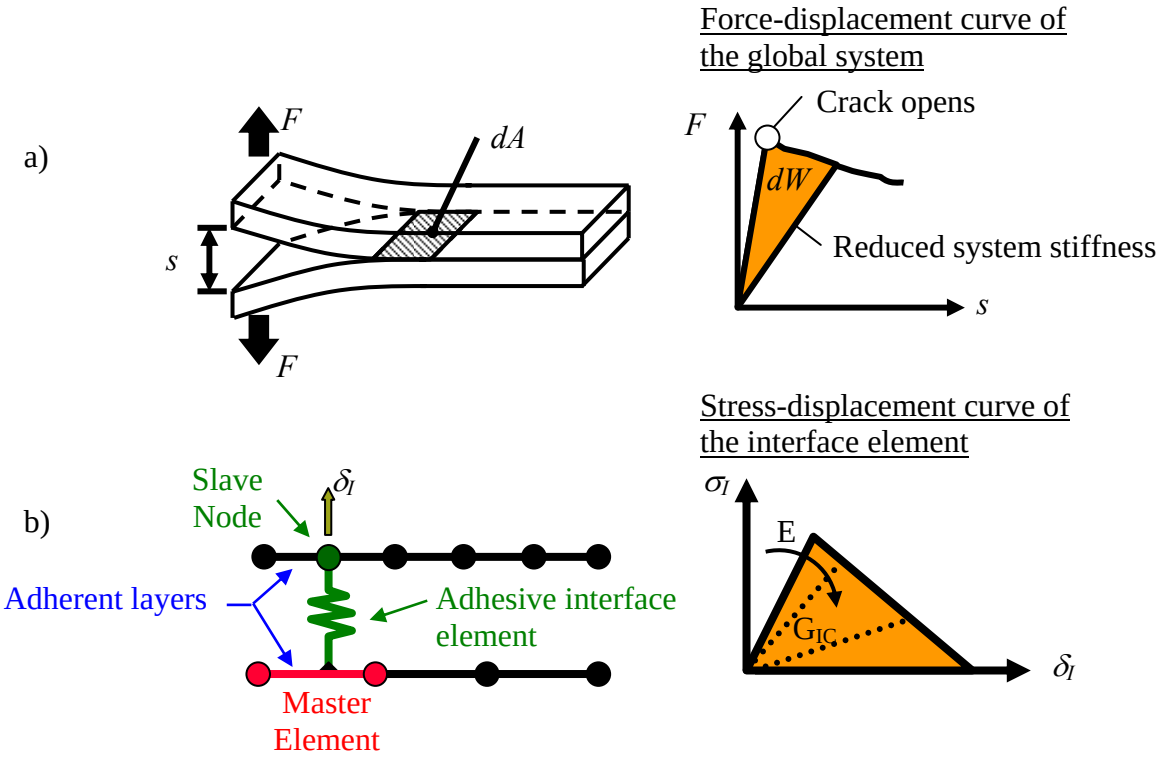

$$G_{IC} = \frac{dW}{dA} = \frac{dW_{Ele}}{dA_{Ele}} = \int \frac{F_I}{A_{Ele}} d\delta_I = \int \sigma_I d\delta_I \qquad (1)$$

Figure 2. Link between Fracture Mechanics and Damage Mechanics for the adhesive interface element demonstrated for pure Mode I loading. Parameter dW is the released elastic energy in the considered system to create a crack of the area dA. The corresponding FE approach defines the absorbed energy W_{Ele} as the area under the stress-displacement curve using a simple triangular stress-displacement relation.

Linear coupling of the strain energy release rates for crack initiation (G_{I0}-G_{II0}) and crack propagation (G_{IC}-G_{IIC}) is assumed between pure Mode I and pure Mode II loading, Figure 3,

$$\frac{G_I}{G_{I0}} + \frac{G_{II}}{G_{II0}} = 1 \quad ; \quad \frac{G_I}{G_{IC}} + \frac{G_{II}}{G_{IIC}} = 1. \qquad (2)$$

For arbitrary combined load paths, the strain energy release rates are decomposed into (G_{IA}, G_{IIA}) for crack initiation and (G_{IB}, G_{IIB}) for complete failure, Figure 3.

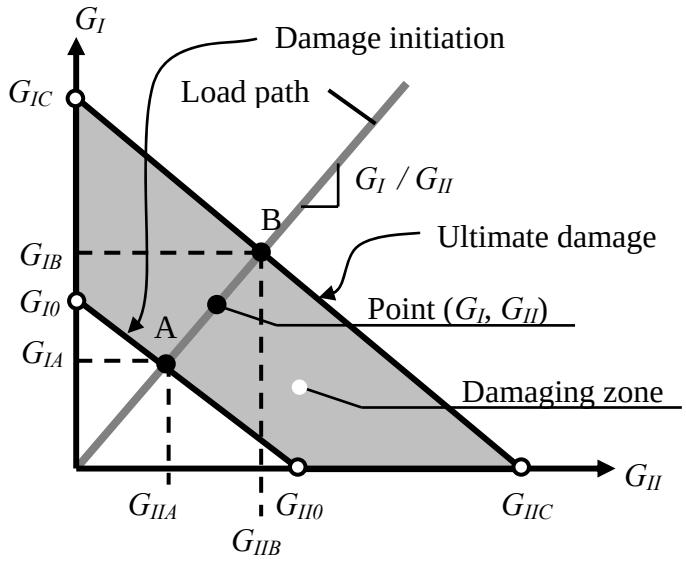

Note: exaggerated display for the initial strain energy release rates G_{i0}. Usually: $G_{i0} << G_{iC}$

Figure 3. Coupling of Mode I and Mode II strain energy release rates for crack initiation and propagation (ultimate damage).

2.1.2. The elastic damaging stress-strain relation

A simple elastic damaging stress-strain relation is used for the interface elements,

$$\begin{Bmatrix} \sigma_I \\ \sigma_{II} \end{Bmatrix} = \begin{bmatrix} E(1-d_I) & 0 \\ 0 & G(1-d_{II}) \end{bmatrix} \begin{Bmatrix} \varepsilon_I \\ \varepsilon_{II} \end{Bmatrix} \quad ; \quad \begin{Bmatrix} \varepsilon_I \\ \varepsilon_{II} \end{Bmatrix} = \frac{1}{t} \begin{Bmatrix} \delta_I \\ \delta_{II} \end{Bmatrix}, \tag{3}$$

where E is the Young's modulus, G is the shear modulus, $d_{I,II}$ are the damage functions, and $\varepsilon_{I,II}$ are the elastic strains.

The following formulae describe Mode I loading. Identical equations can be established for Mode II by interchanging indices I with II and the out-of-plane modulus E with the in-plane shear modulus G, respectively.

A simple triangular shape is imposed for the elastic damaging stress-strain relation, Figure 4. Point A represents damage initiation and point B represents the fully damaged state (d_I = 1) for arbitrary combined loading. The strains for crack initiation, $\varepsilon_{IA,}$, and ultimate failure, ε_{IB}, follow from the requirement of letting the area under the stress-displacement curve equal the corresponding strain energy release rate, $G_{IA,B}$ (as explained in Figure 2):

$$G_{IA,B} = \frac{1}{2}\sigma_I^{\max}\delta_{IA,B} = \frac{1}{2}\sigma_I^{\max}\varepsilon_{IA,B}t \quad \Rightarrow \quad \varepsilon_{IA,B} = \frac{2G_{IA,B}}{\sigma_I^{\max}t}. \tag{4}$$

For pure Mode I loading $G_{IA,B}$ corresponds to $G_{I0,C}$.

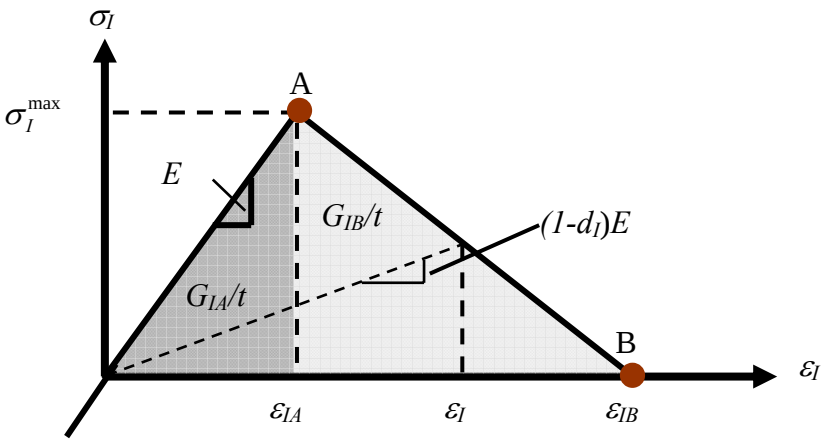

Figure 4. Triangular stress-strain relation and graphical representation of the energy release rates shown for Mode I loading.

The imposed triangular shape of the stress-strain relation leads to the following definition of the damage function:

$$d_I = \begin{cases} \sup_{t\le\tau}\left\langle \dfrac{\varepsilon_{IB}\left(\varepsilon_I(\tau)-\varepsilon_{IA}\right)}{\varepsilon_I(\tau)\left(\varepsilon_{IB}-\varepsilon_{IA}\right)}\right\rangle_+ & if\left(\varepsilon_I(\tau)>0\right) \\ 0 & otherwise \end{cases}, \tag{5}$$

where it has to be noted that, according to the definition, no damage occurs under Mode I compression loading. In the case of unloading, the stress-strain curve intersects the origin (no plastic deformation), Figure 4. This distinction is irrelevant for shear (Mode II) loading.

2.1.3. The fracture criterion for crack initiation

According to Figure 4, the following relation of stresses and corresponding strain energy release rates exists at the threshold to crack initiation and below:

$$G_I = t\int_0^{\varepsilon_I}\sigma_I d\varepsilon_I = \frac{t\langle\sigma_I\rangle_+^2}{2E} \quad\Rightarrow\quad G_{I0} = \frac{t\left(\sigma_I^{max}\right)^2}{2E}, \tag{6}$$

where only positive tensile stresses contribute to potential fracture initiation. Using equation (2) and substituting the energy release rates by the expressions in terms of stresses, equation (6), yields the non-symmetric quadratic stress failure locus for crack initiation,

$$\left(\frac{\langle\sigma_I\rangle_+}{\sigma_I^{max}}\right)^2 + \left(\frac{\sigma_{II}}{\sigma_{II}^{max}}\right)^2 = 1, \tag{7}$$

where maximum tensile and shear stresses, σ_I^{max} and σ_{II}^{max}, have to be determined by experiments.

2.2. The detailed modelling approach (Solid element modelling)

The DF model [7] provides the foundation of the solid element approach and is enhanced to address unsymmetrical yield and strain rate hardening. The enhanced DF model operates in conjunction with the JC fracture criterion [8] and has been implemented in a user subroutine of the commercial crash code PAM-CRASH™ [16].

2.2.1. Stress-strain relation

Isotropic behaviour is assumed for the adhesive material. The corresponding relation between stresses and $\boldsymbol{\sigma}$ and elastic strains $\boldsymbol{\varepsilon}^{e}$ is

$$\boldsymbol{\sigma} = \mathbf{E}\boldsymbol{\varepsilon}^{e}, \tag{8}$$

where $\mathbf{E}$ is the symmetric 6x6 stress-strain matrix ($E_{ij} = E_{ji}$), with

$$\begin{aligned} &E_{11} = E_{22} = E_{33} = \left(1-\nu^{e}\right)c; \\ &E_{44} = E_{55} = E_{66} = G; \\ &E_{12} = E_{23} = E_{31} = \nu^{e}c; \\ &c = \frac{E}{\left(1+\nu^{e}\right)\left(1-2\nu^{e}\right)} \quad ; \quad G = \frac{E}{2\left(1+\nu^{e}\right)}. \end{aligned} \tag{9}$$

Parameter E is the elastic modulus, G is the shear modulus, and ν^{e} is the elastic Poisson's ratio.

2.2.2. Yield condition, strain rate hardening, and flow rule

Yield condition

For isotropic materials it is convenient to use invariant stress and strain tensor expressions for modelling plastic deformation and fracture. The hydrostatic stress, σ_m, is related to the first invariant of the stress tensor I_1:

$$\sigma_m = \frac{1}{3} Tr\, \boldsymbol{\sigma} = \frac{I_1}{3}, \tag{10}$$

whereas the second invariant of the deviator stress tensor, J_2, is related to the equivalent von Mises stress σ_e,

$$\sigma_e = \sqrt{\frac{3}{2}\sigma'_{ij}\sigma'_{ij}} = \sqrt{3J_2} \quad ; \quad \boldsymbol{\sigma}' = \boldsymbol{\sigma} - \sigma_m \mathbf{I}. \tag{11}$$

The enhanced DF yield criterion is

$$\Phi = \tilde{\sigma} - B \le 0, \tag{12}$$

where $\tilde{\sigma}$ is the effective equivalent stress,

$$\tilde{\sigma}^2 = \sigma_e^{\,2} + \alpha^2\left(\sigma_m - \sigma_0\right)^2, \tag{13}$$

which is a function of the von Mises equivalent stress and of the hydrostatic stress. The yield function Φ takes the shape of an ellipse in the σ_e-σ_m stress space, Figure 5, defined by B and $A = B/\alpha$. Parameter σ_0 allows improved adjustment to experimental observations by shifting the ellipse along the σ_m-axis.

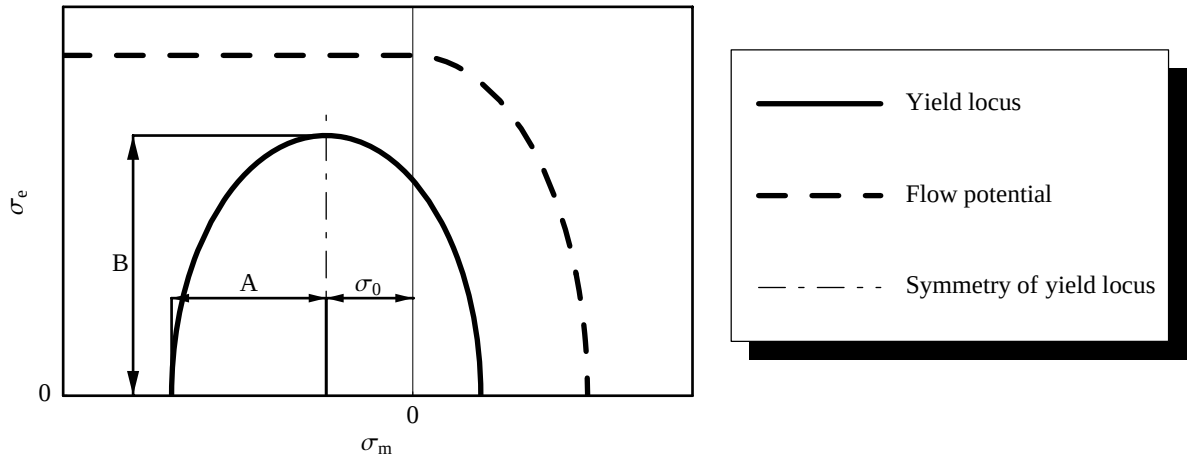

Figure 5. Principle plot of the yield locus and the flow potential in the stress invariant space represented by σ_m and σ_e.

Strain hardening and strain rate hardening

The quasi-static true tensile stress versus plastic tensile strain hardening curve $\sigma_T^{sta}\left(\varepsilon_T^p\right)$ can be obtained by a quasi-static tension test of an adhesive coupon. Any monotonically increasing curve function can be input. A direct relation exists between uniaxial tensile stress σ_T and yield function parameter B, using equation (12) with $\sigma_e = \sigma_T$, and $\sigma_m = \sigma_T/3$:

$$B = \sqrt{1+\alpha^2\left(\frac{1}{3}-\frac{\sigma_0}{\sigma_T}\right)^2}\,\sigma_T\,. \tag{14}$$

For addressing strain rate hardening a simple logarithmic model is proposed [8],

$$\sigma_T\left(\varepsilon_T^p,\dot{\varepsilon}_T^p\right)=\begin{cases}\left[1+C\ln\left(\dfrac{\dot{\varepsilon}_T^p}{\dot{\varepsilon}_0^p}\right)\right]\sigma_T^{sta}\left(\varepsilon_T^p\right) & if\left(\dot{\varepsilon}_T^p > \dot{\varepsilon}_0^p\right)\\ \sigma_T^{sta}\left(\varepsilon_T^p\right) & otherwise\end{cases}, \tag{15}$$

where C is a fitting parameter, $\dot{\varepsilon}_T^p$ is the plastic tensile strain rate, and $\dot{\varepsilon}_0^p$ is the plastic tensile strain rate threshold below which the static yield stress $\sigma_T^{sta}\left(\varepsilon_T^p\right)$ is used.

Flow potential and flow rule

A non-associated flow rule is used to address non-conservation of the volume observed for the adhesive material (see section 3.1), where the flow potential is defined by an unsymmetrical elliptic function,

$$G = \sqrt{{\sigma_e}^2+\beta^2\left\langle\sigma_m\right\rangle_+^2}\quad;\quad \dot{\varepsilon}_{ij}^p = \dot{\lambda}\frac{\partial G}{\partial\sigma_{ij}}, \tag{16}$$

where β is the shape parameter, and $\dot{\lambda}$ is the plastic multiplier. Negative hydrostatic stresses do not contribute to plastic flow, Figure 5.

Fracture Criterion

The JC fracture criterion [8] is based on the idea of accumulated damage, defined as the ratio of equivalent von Mises plastic strain increments $d\varepsilon^p$ to the corresponding failure strain ε_f,

$$D = \int \frac{d\varepsilon^p}{\varepsilon_f} \quad ; \quad d\varepsilon^p = \sqrt{\frac{2}{3}\dot{\varepsilon}_{ij}^p \dot{\varepsilon}_{ij}^p}\; dt \tag{17}$$

where Δt is the time increment and the plastic failure strain is an exponential function of the stress triaxiality σ_m/σ_e,

$$\varepsilon_f = d_1 + d_2\, e^{-d_3 \frac{\sigma_m}{\sigma_e}}. \tag{18}$$

Damage occurs once the accumulated damage exceeds $D = 1$.

3. Material model parameter identification procedure

The material model parameters for the simplified interface approach and the detailed solid element approach are obtained from the same set of experiments. The high strength epoxy adhesive Betamate™ 1496 [2] is used for all tests. The whole set of material model parameters is summarised in Appendix Table 1.

3.1. Uniaxial tension and compression tests using adhesive specimens

The quasi-static mechanical properties of Betamate™ can be obtained by several sources, e.g. [18], where usually simple adhesive tension and compression coupons were used. Some experimental results for dynamic tension loading are also published, e.g. [19] or [20]. The basic elastic and yield material properties obtained from these sources are summarised in Appendix Table 1.

The shape parameter β for the modified Fleck model can be obtained from the plastic Poisson's ratio ν^p in a tension test. Using equation (16) yields

$$\nu^p = -\frac{\Delta\varepsilon_1^p}{\Delta\varepsilon_2^p} = \frac{\frac{1}{2} - \left(\frac{\beta}{3}\right)^2}{1 + \left(\frac{\beta}{3}\right)^2} \quad \Rightarrow \quad \beta = \frac{3}{\sqrt{2}}\sqrt{\frac{1-2\nu^p}{1+\nu^p}}, \tag{19}$$

For Betamate™, a ν_p = 0.23 has been measured, corresponding to β = 1.4. The quasi-static hardening curve is approximated by a linear function, Figure 6a, and the strain rate model fitting parameter C = 0.36 can be determined using equation (15), Figure 6b.

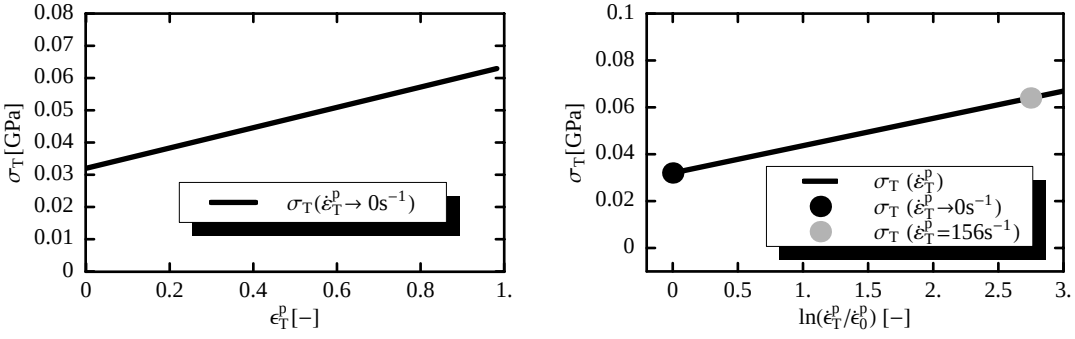

a) b)

Figure 6. Quasistatic hardening curve and strain rate hardening for Betamate 1496: a) quasi-static hardening curve approximated from uniaxial tension adhesive coupon testing [18]; b) approximated logarithmic strain rate mode (yield stresses are obtained from literature sources [20]).

3.2. Fracture Toughness testing using the Double Cantilever Beam

Quasi-static Mode I fracture toughness testing using the Double Cantilever Beam test (DCB) [21] is a widely accepted test procedure for measuring the critical strain energy release rate G_{IC} for quasi-brittle materials, e.g. composites. More recently, the test procedure has been adopted for adhesive testing, e.g. ([22], [23]). The critical strain energy release rate is input to the interface model only

Two aluminium beams are adhesively bonded, Figure 7, imposing an adhesive layer thickness of t = 0.5mm. According to the test standard an artificial initial crack is introduced by a polyimide film insert, having a thickness of 12.5μm.

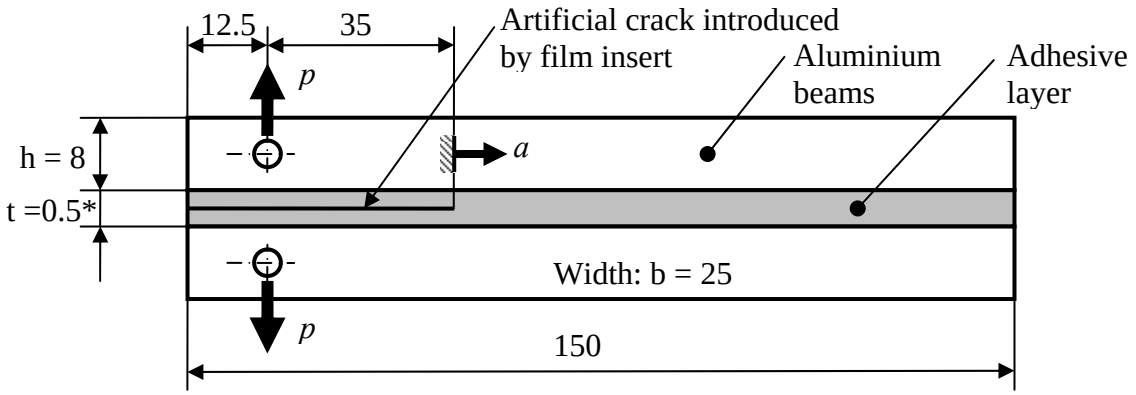

*) Not drawn to scale

Figure 7 Specimen dimensions (in mm) of the Double Cantilever Beam (DCB) specimen for quasi-static Mode I adhesive fracture toughness testing.

According to the test standard the specimens are tested on an Instron 5500R tensile testing machine. The applied force p and the crack propagation distance a are monitored and recorded. The critical strain energy release rate can be estimated by classical beam theory,

$$G_{IC} = \frac{4p^2}{E_{Al}h^2}\left(\frac{3a^2}{h^3}+\frac{1}{h}\right), \tag{20}$$

where E_{Al} = 70GPa is the Young's modulus for aluminium. A Finite Element model of the DCB test is established, Figure 8, where the thick aluminium beams are represented by solid elements, whereas the adhesive layer is discretised using interface elements. The material model parameters summarised in Appendix Table 1 are applied. The critical strain energy release rate of G_{IC} = 5kJ/m² leads to a very good agreement of the force-displacement curves in comparison with the experiments, Figure 9. The critical strain energy release rate under Mode II is estimated, G_{IIC} = 10kJ/m². The strain energy release rates are considered strain rate independent in this study. However, it has to be noted that strain rate dependency has been indicated within an ongoing project [10].

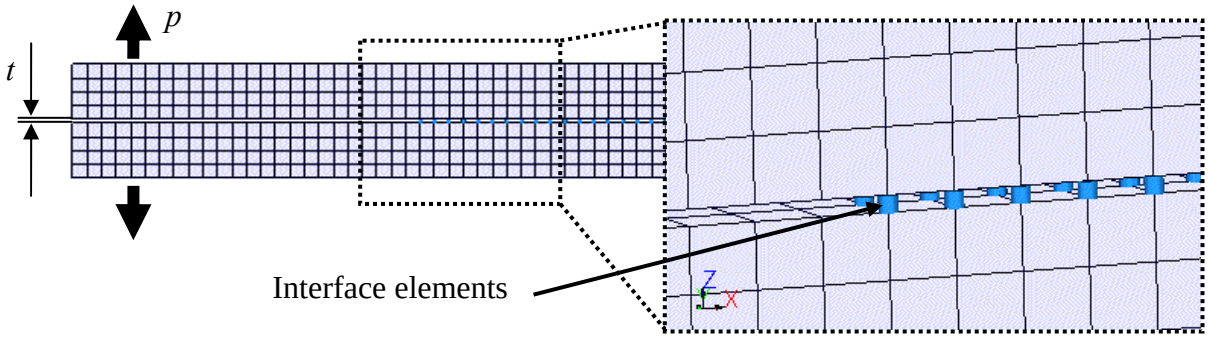

Figure 8. Finite Element discretisation of the Double Cantilever Beam specimen using interface elements for the representation of the adhesive layer.

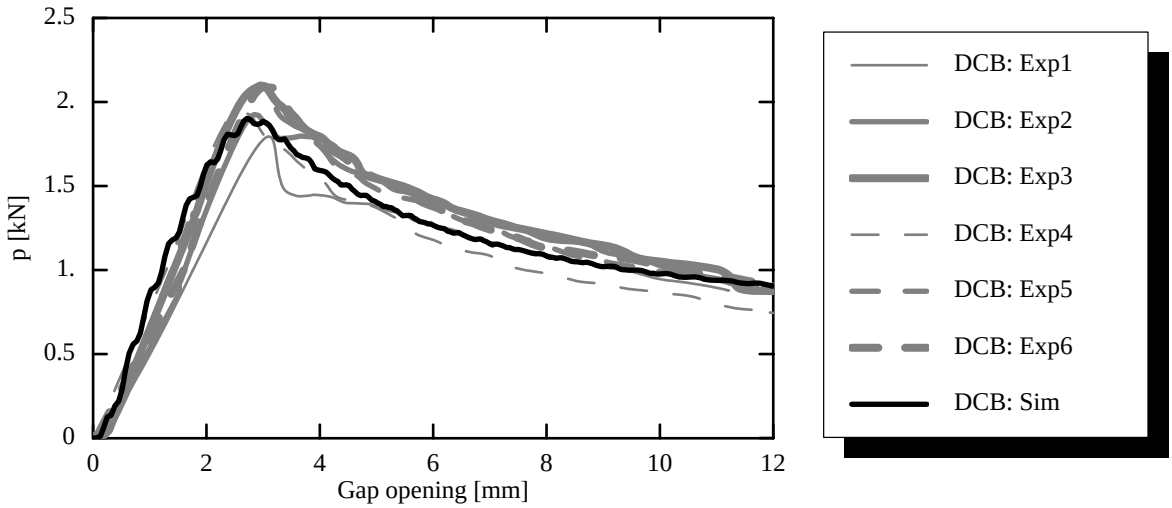

Figure 9. Force-displacement curves of Mode I fracture toughness tests using the Double Cantilever Beam specimen: Comparison of experimental and simulation results.

3.3. Adhesively butt-joined tubes subjected to combined quasi-static loading

Adhesively butt-joined thin-walled cylindrical tubes are utilised for the mechanical characterisation of thin adhesive layers under pure and combined quasi-static tension and torsion loading, Figure 10.

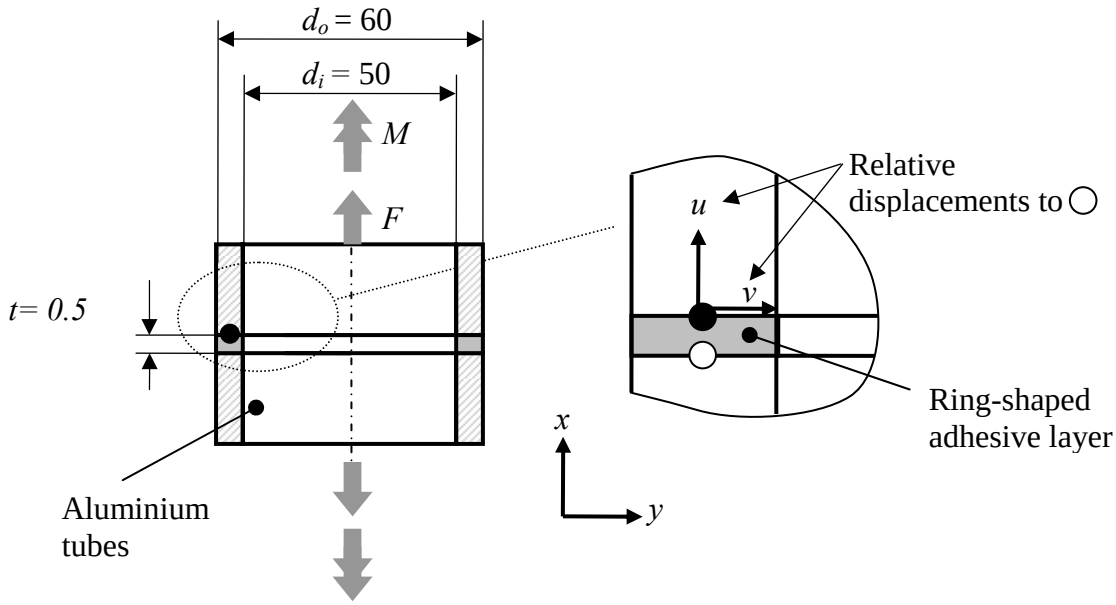

Figure 10. Combined tension/torsion device for quasi-static testing of thin adhesive layers (dimensions in mm).

The nominal stresses and strains are calculated from the measured forces and moments (F, M) and displacements (u, v):

$$\sigma_x = \frac{F}{A} = \frac{4F}{\pi\left(d_o^{\,2} - d_i^{\,2}\right)} \quad ; \quad \varepsilon_x = \ln\left(1+\frac{u}{t}\right)$$
$$\tau_{xy} = \frac{M}{W} = \frac{16Md_o}{\pi\left(d_o^{\,4} - d_i^{\,4}\right)} \quad ; \quad \gamma_{xy} = \arctan\left(\frac{v}{t+u}\right) \tag{21}$$

The tests are performed quasi-statically imposing a principal strain rate of 0.001/s on an MTS 809.55 biaxial tension/torsion test machine. Different strain ratios, $R = \gamma_{xy}/\left(2\varepsilon_x\right) = const$, were investigated: R = 0 (pure tension), R = 1/2, R = 2, R = ∞ (pure torsion). The obtained stress-strain curves are shown in Figure 11-Figure 16. Yield (σ_x^Y, τ_x^Y) and maximum (σ_x^M, τ_x^M) stresses are obtained by curve analysis.

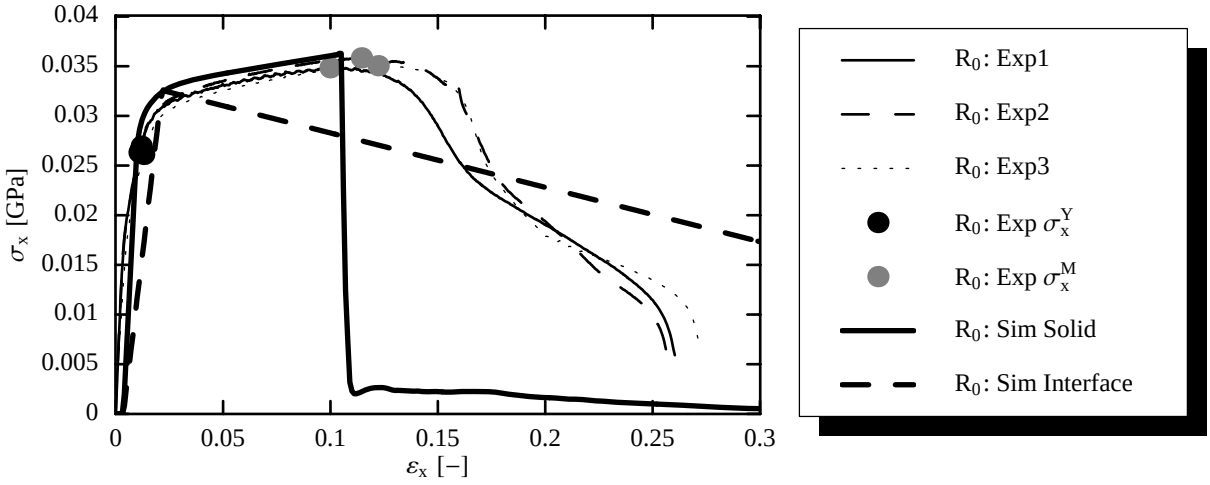

Figure 11. Adhesively butt-joined tubes subjected to quasi-static pure tensile loading (R = 0): comparison of axial stress-strain curves of experiments and simulations.

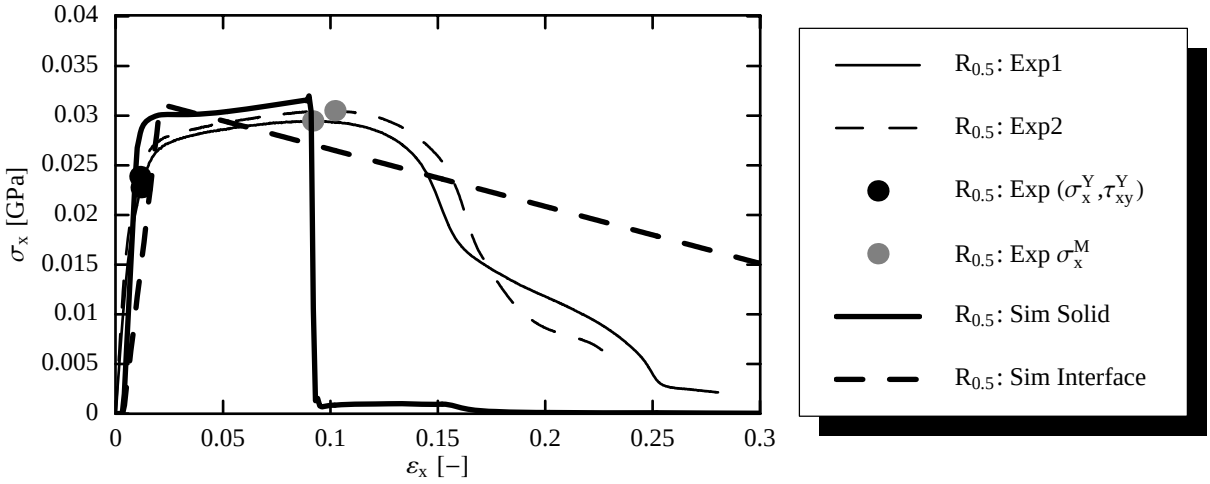

Figure 12. Adhesively butt-joined tubes subjected to quasi-static combined loading (R = 1/2): comparison of axial stress-strain curves of experiments and simulations.

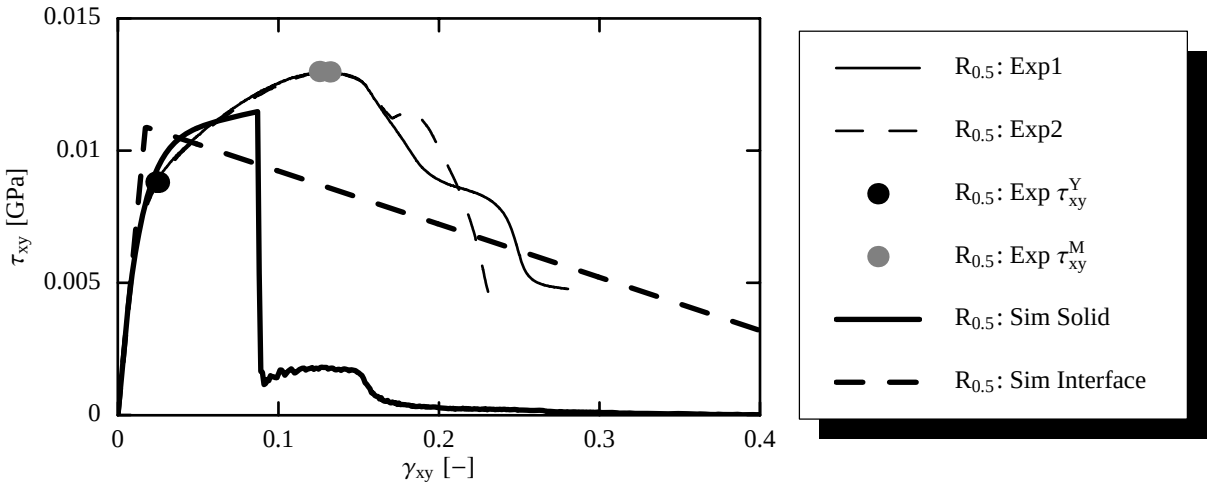

Figure 13. Adhesively butt-joined tubes subjected to quasi-static combined loading (R = 1/2): comparison of shear stress-strain curves of experiments and simulations.

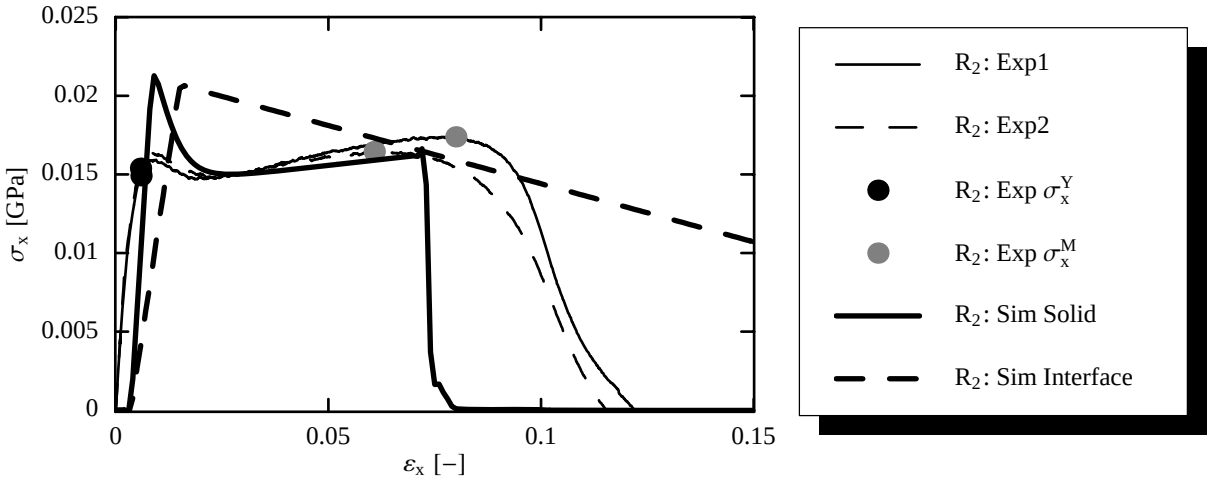

Figure 14. Adhesively butt-joined tubes subjected to quasi-static combined loading (R = 2): comparison of axial stress-strain curves of experiments and simulations.

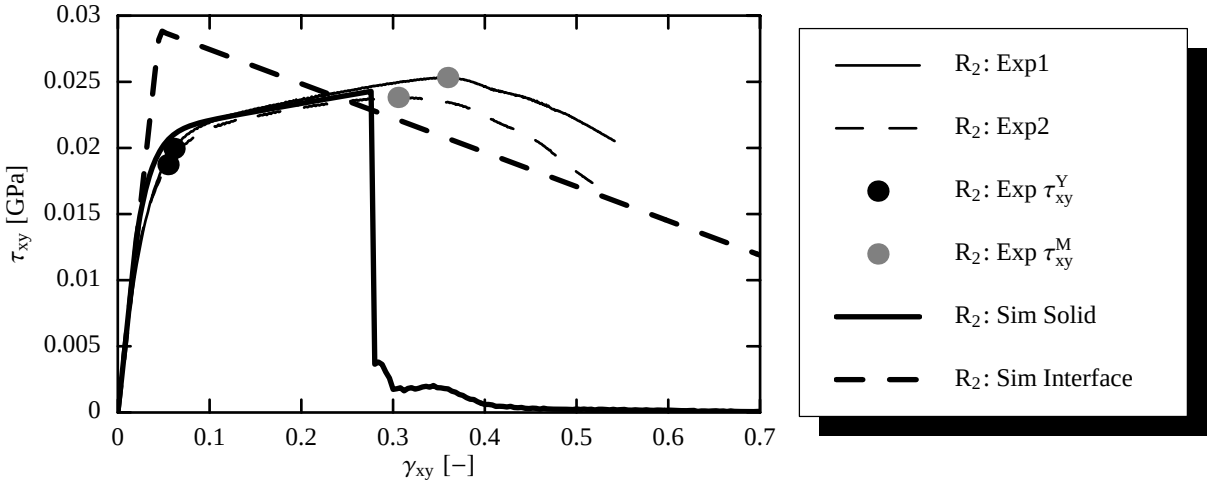

Figure 15. Adhesively butt-joined tubes subjected to quasi-static combined loading (R = 2): comparison of shear stress-strain curves of experiments and simulations.

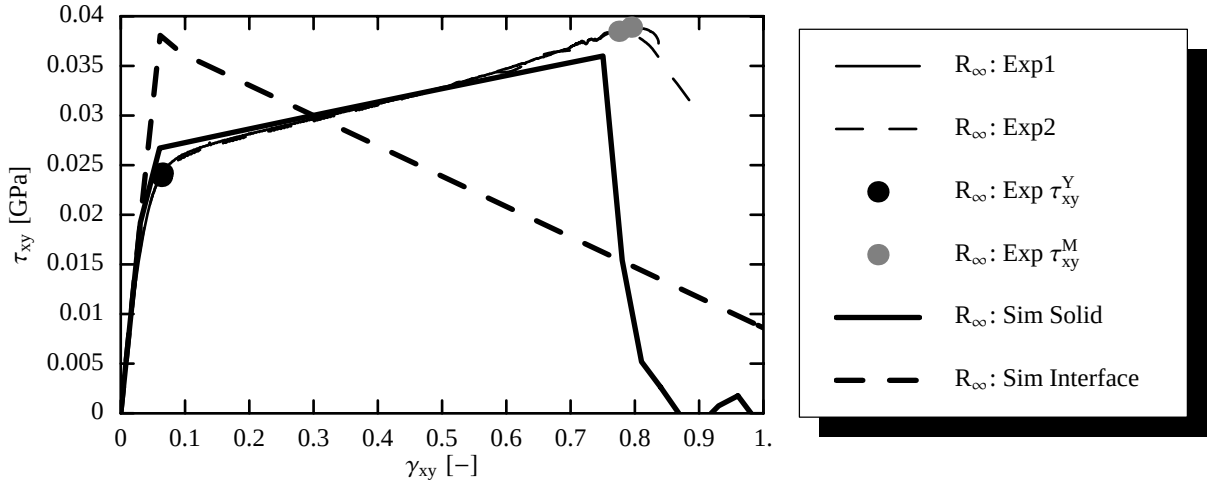

Figure 16. Adhesively butt-joined tubes subjected to quasi-static pure shear loading (R = ∞): comparison of shear stress-strain curves of experiments and simulations.

3.3.1. Finite Element modelling of the adhesively butt-joined tubes

Finite Element simulation models of the adhesively butt-joined tubes are established, where only the ring-shaped adhesive layer is modelled, whereas the aluminium tubes are considered quasi-rigid and are represented by rigid shell layers on top and at the bottom of the adhesive layer, Figure 17. For the interface model the Node-To-Element connections are visualised by bar elements, Figure 17 section (a), whereas for the solid element model the adhesive layer is discretised by four layers of solid elements distributed over the thickness, Figure 17 section (b).

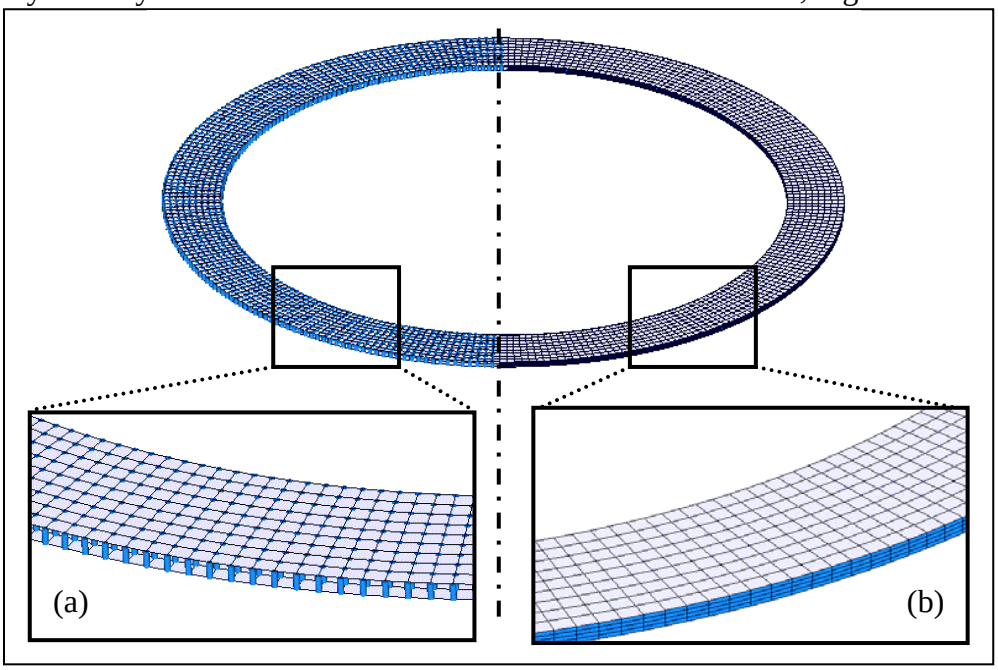

Figure 17. Finite Element simulation models of the adhesively butt-joined aluminium tubes. The ring-shaped adhesive layer is represented by: (a) simple node-to-element interface elements visualised by bar elements; (b) four layers of solid elements distributed over the adhesive layer thickness.

3.3.2. Model parameter identification for the interface model

The quadratic stress failure criterion for interface crack initiation has been discussed in section 2.1.3. The maximum stresses of the adhesively joined tube experiments in normal (Mode I) and shear (Mode II) direction are used to determine the fracture locus. Considering $\sigma_I = \sigma_x^M$ and $\sigma_{II} = \tau_{xy}^M$, the stresses are collected in one chart, Figure 18 and can be reasonably approximated by the quadratic stress failure criterion, equation (7). Fitting parameters $\sigma_I^{\max}$ and $\sigma_{II}^{\max}$ are determined by a least square fitting operation and are summarised in Appendix Table 1. The tube simulations are evaluated using the determined maximum stress parameters and the critical strain energy release rates obtained in the previous section, Figure 11-Figure 16. The maximum stresses can be well predicted whereas, as expected due to the simplified pure elastic constitutive law of the interface elements, the plastic domain can not be accurately represented. The post-peak domain is characterised by the critical strain energy release rates and the imposed triangular stress-strain relation.

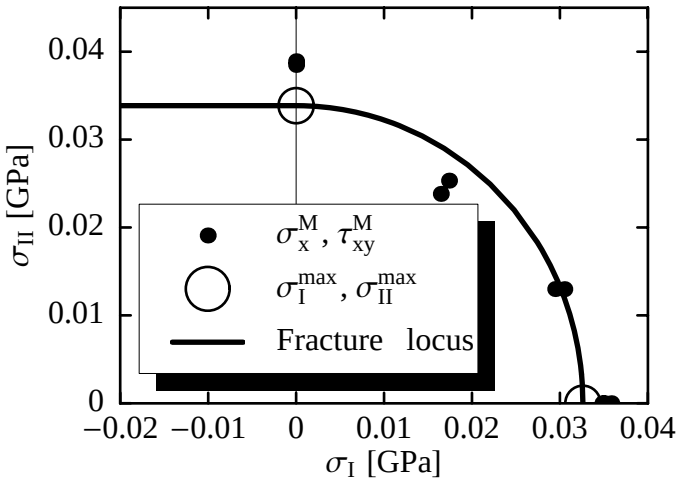

Figure 18. Approximation of the quadratic stress failure curve for interface crack initiation: fitting through the maximum stresses obtained from the adhesively butt-joined tube tests.

3.3.3. Model parameter identification for the solid element model

Determination of the yield locus parameter

Assuming quasi-homogeneous stress distribution and plain strain in the adhesive layer the stress tensor at the threshold to yielding is [18]:

$$\boldsymbol{\sigma} = \begin{bmatrix} \sigma_x^Y & \tau_{xy}^Y & 0 \\ \tau_{xy}^Y & \kappa\sigma_x^Y & 0 \\ 0 & 0 & \kappa\sigma_x^Y \end{bmatrix} \quad ; \quad \kappa = \frac{\nu^e}{1-\nu^e}, \tag{22}$$

where σ_x^Y and τ_{xy}^Y are the tensile and shear yield stresses, respectively. For each stress-strain curve in Figure 11-Figure 16 the yield stresses can be transformed into the invariant stress space using equations (10) and (11):

$$\sigma_m = \frac{1+2\kappa}{3}\sigma_x^Y \quad ; \quad \sigma_e = \sqrt{(1-\kappa)^2\left(\sigma_x^Y\right)^2 + 3\left(\tau_{xy}^Y\right)^2}\,. \tag{23}$$

The yield points of all adhesively butt-joined tubes, accompanied by the yield points of the uniaxial tension and compression tests, are shown in Figure 19. The quasi-static yield locus can be well approximated using equations (12) and (14), where fitting parameters α and σ_0 are determined by a least square fitting method. The yield locus for dynamic uniaxial tensile loading at $\dot{\varepsilon}_T^p = 156 s^{-1}$ is also included in the figure.

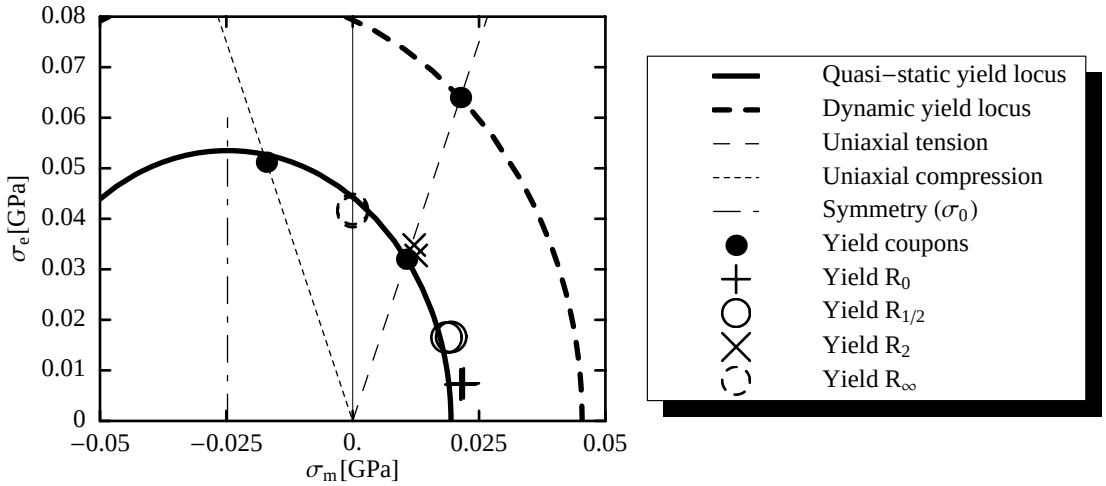

Figure 19. Approximation of the yield locus for the high strength epoxy adhesive Betamate™ 1496 using the enhanced DF model.

Determination of the fracture model parameters

An inverse approach is used for the determination of the JC fracture parameters. The different strain ratios (R = 0, ½, 2, ∞) are applied to the simulation model. The stress-strain curves of the butt-joined tubes display a stress maximum after which the material softens and the stresses gradually drop, Figure 11-Figure 16. This softening phase will be neglected by the Johnson-Cook fracture model. Hence, the maximum stresses are assumed to define the state of fracture initiation. Each simulation is run to this state, where the fracture criterion is being deactivated. At the corresponding state of failure, the computed equivalent von Mises plastic strains and the corresponding stress triaxialities of the elements close to the inner ring boundary and close to the outer ring boundary, which potentially cause fracture initiation, are collected in one chart, Figure 20. These data points can be well approximated by equation (18), where the parameters d_1, d_2, and d_3 are determined by a least square fit (see Appendix Table 1).

For confirmation, the simulations are repeated, now using the determined parameters for the fracture criterion. A good agreement of computed and experimental stress-strain relations is observed for most of the load cases, Figure 11-Figure 16, including the prediction of initial elastic stiffness, yield stress, elasto-plastic deformation, and failure. It has to be noted that the predicted initial normal stress peak for the R=2 simulation, Figure 14, is significantly higher than in the experiment, It can be shown that using a better (non-linear) approximation of the hardening curve reduces this discrepancy.

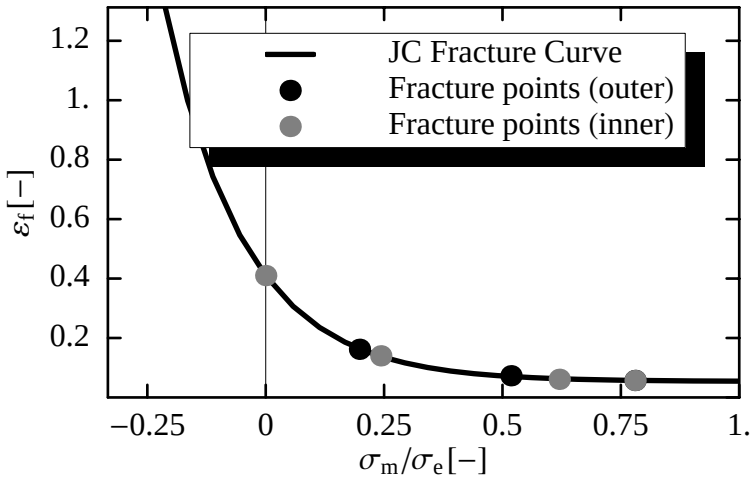

Figure 20. Approximation of the Johnson-Cook fracture curve for the high strength epoxy adhesive Betamate™ 1496.

4. Validation testing and simulation

For validation and final comparison of the established modelling techniques, a more complex adhesively joined structure is investigated. Two aluminium extrusions are adhesively bonded, using one flat and two L-shaped supporting assembly parts, Figure 21 and Figure 22. The large extrusion is fixed and the smaller extrusion is subjected to quasi-static and dynamic loading. For quasi-static loading a load cell in the punch records the force, whereas the displacement is measured using a laser extensometer. The relative displacement of the punch with respect to the large extrusion is measured. This avoids potential measurement errors introduced by rotation of the whole set-up due to bending of the mounting plate.

For dynamic testing an impactor with a weight of m = 12.5kg and an impact velocity of v = 4m/s is utilised. The force and displacements are computed by integration of the recorded acceleration measured in the impactor. In this case the rotation effect of the set-up can not be performed. Hence, the results of quasi-static and dynamic testing can not be truly compared.

For numerical simulation of the tests, an FE model is established, using shell elements for the representation of the extrusions. The thicker supporting parts are discretised by solid elements, Figure 22. For the simplified modelling approach the adhesive layer is represented by interface elements, whereas for the detailed modelling approach the adhesive layer is represented using one layer of solid elements.

It has to be noted that no congruent meshes are required for both approaches. For the solid element approach, the connection between adhesive layer and the aluminium extrusions and supporting parts is achieved by using additional mesh independent quasi-rigid tied interfaces without failure criterion, Figure 22.

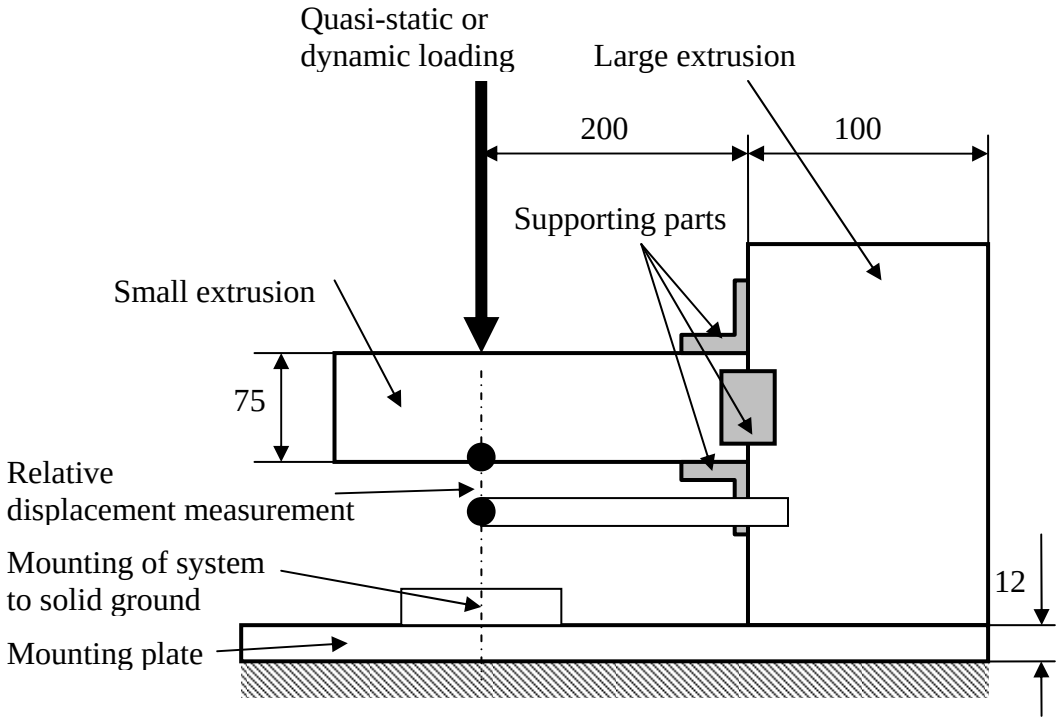

Figure 21. Sketch (dimensions in mm) of the adhesively bonded aluminium extrusions using two L-shaped and one flat supporting parts; all adhesive layers have a thickness of 0.5mm and a width of 15mm.

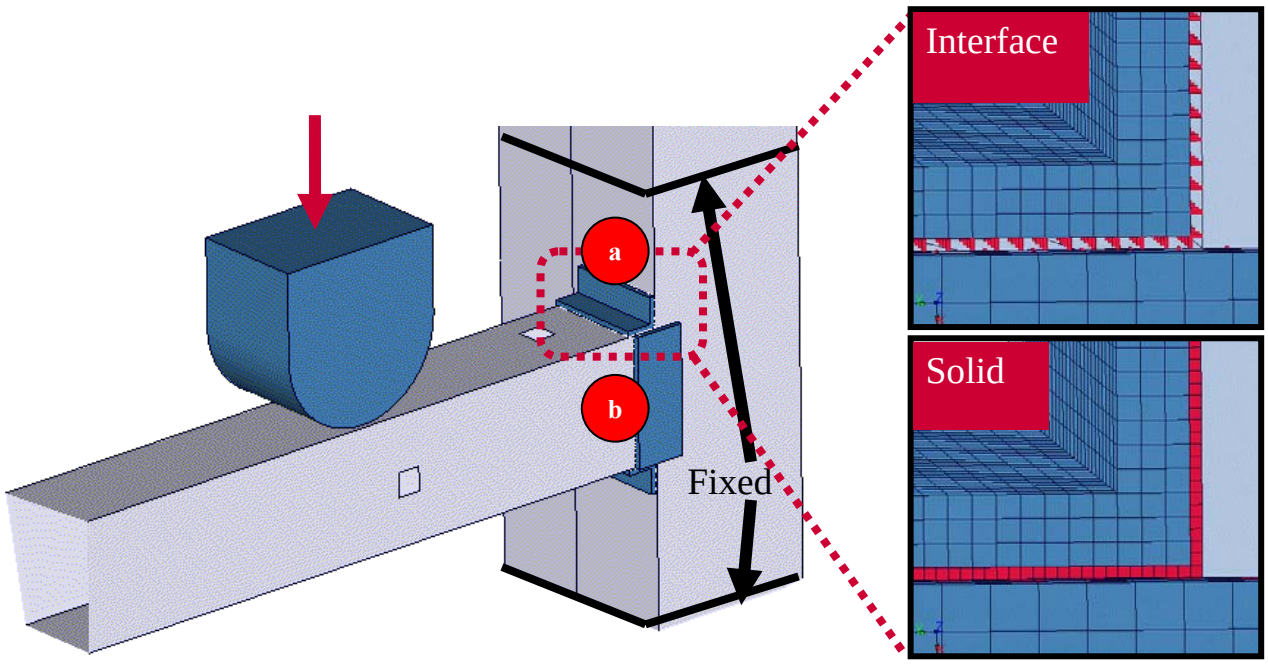

Figure 22. Finite Element model and different modelling approaches for the adhesively bonded aluminium extrusions subjected to quasi-static and dynamic loading.

Quasi-static loading

The experimental force-displacement curves are displayed in Figure 23, accompanied by the simulation results using the interface and the solid element approach. Structural failure of the joined extrusions is governed by adhesive failure occurring in a sequence of two phases. In the

first phase, the upper L-shaped supporting part, Figure 22 (position a), gradually peels off. This phase is characterised by the transition of a linear elastic response to a strongly nonlinear relation of force and displacement in Figure 23. In the second phase the adhesive layer beneath the flat supporting part, Figure 22 (position b), fails due to shear loading, characterised in Figure 23 by decreasing load prior to part separation. The experimental force-displacement curves exhibited some scatter, where the results of both simulation approaches tend toward the experiment having the lowest maximum load, Figure 23. Both numerical approaches predict the correct sequence of failure according to the experiments.

The interface element approach can predict the initial stiffness. However, it can not reproduce the following nonlinear relation of force and displacement. The predicted response is brittle and the maximum force is slightly overrated. Nevertheless, the overall agreement of this strongly simplified approach is encouraging.

The solid element approach leads to slightly lower elastic stiffness prediction in comparison to the experiment. This effect is due to the finite stiffness of the additional elastic tied interfaces between the adhesive layer and the aluminium parts. The stiffness of these elastic spring elements depends on the solution time step and increases as the time step decreases [16]. A principle study is added in Figure 23, in which the solution time step is artificially reduced by factor 10. Now, the initial elastic stiffness can be well predicted; however, at an expense of a significantly higher computation time.

In contrast to the interface approach, the solid element approach can represent the nonlinear force-displacement relation prior to structural failure, where the maximum force level is slightly underestimated.

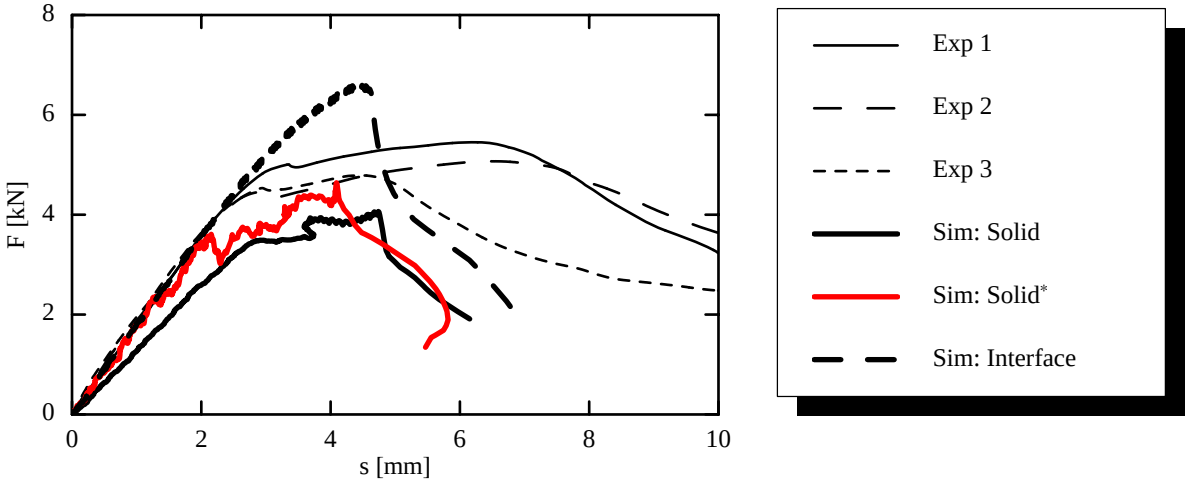

*) Imposing increased penalty spring stiffness of elastic tied interfaces due to reduced solution time step

Figure 23. Force-displacement curves of adhesively joined aluminium extrusions subjected to quasi-static loading: comparison of experimental and simulation results.

Dynamic loading

Good repeatability of the experiments has been observed, Figure 24. The initial contact force peak is followed by a force drop after which the force increases again and remains level until complete structural failure. The same sequence of structural adhesive failure is observed for the dynamic and quasi-static tests.

The numerical computations using the interface and the solid element approach (with and without strain rate dependency) can predict the general trend of the experimental force displacement relation, Figure 25, where all simulations predict slightly amplified dynamic noise in the first phase of the impact. A potential reason is the lack of physical damping in the computation models.

The interface approach and the solid element approach using the strain rate hardening model predict higher force plateaus after the initial force peak than those observed in the experiments. Due to the higher force level the initial kinetic energy introduced to the system is insufficient to cause complete adhesive failure. A rebound is observed in the simulation at approximately 14mm displacement.

For the interface approach the higher force level can be explained by the negligence of plastic deformation. For the solid element approach using strain rate hardening, the higher force level could be due to the negligence of strain rate dependent fracture. Under dynamic loading the adhesive potentially embrittles, which is not taken into account in the simulation model. Interestingly, the solid element approach without strain rate hardening is in very good agreement with the experiments. This would be explained by the assumption that higher dynamic strength is compensated by lower dynamic failure strain.

Analogous to the quasi-static test, the results using the simplified interface model are encouraging.

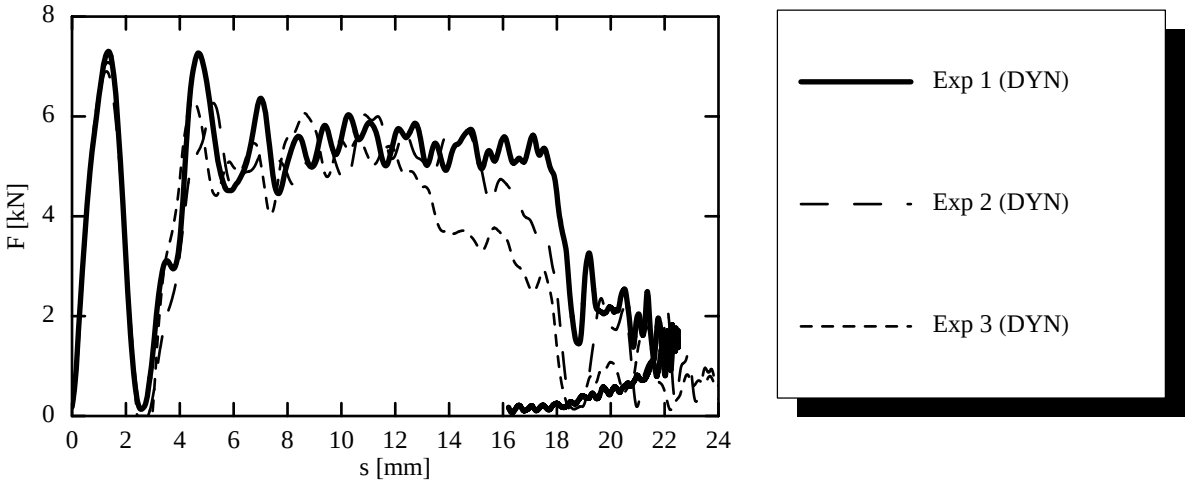

Figure 24. Experimental force-displacement curves of an adhesively joined aluminium extrusions assembly subjected to dynamic loading.

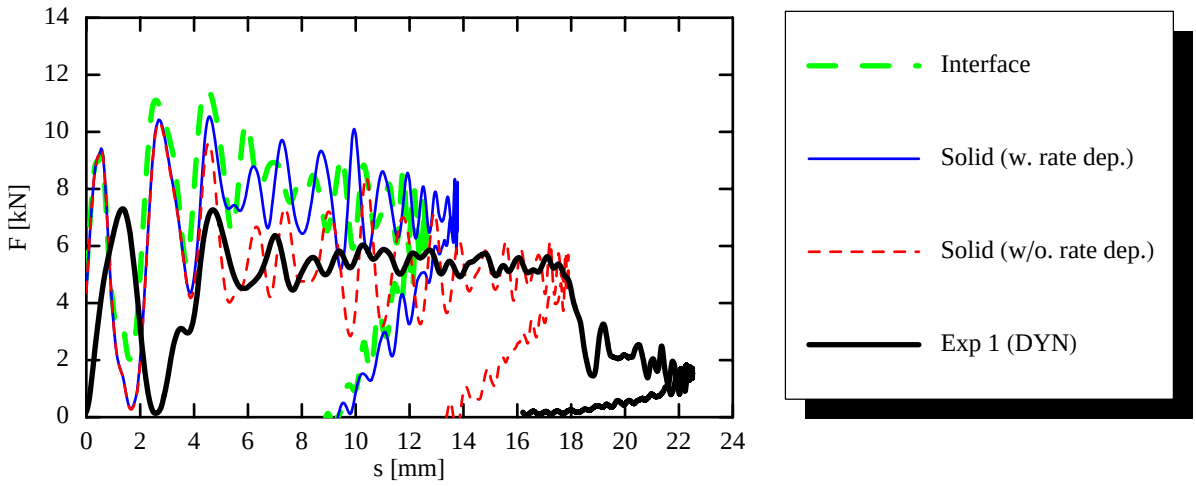

Figure 25. Force-displacement curves of an adhesively joined aluminium extrusions assembly subjected to dynamic loading: comparison of experimental and simulation results (using moving average filter).

5. Conclusions

A new 3D material model for high strength adhesives has been developed and implemented in the explicit crash code PAM-CRASH™ as a user subroutine. It enhances the work by Deshpande and Fleck, incorporates the fracture criterion by Johnson and Cook and covers the specific material behaviour of thin layered high strength epoxy adhesive joints, including hydrostatic stress dependent yield and failure, non-symmetric yield and plastic flow, and strain rate hardening. Furthermore, an existing node-to-element interface model has been investigated, which originally has been developed for the simulation of delamination of quasi-brittle composites. The interface model uses a simplified elastic damaging law including a stress based failure criterion for crack initiation and an energy based criterion for crack propagation.

The required material model parameters for both approaches are obtained from a comprehensive test programme, including uniaxial and multiaxial loading, and fracture toughness testing.

A validation example, using two adhesively joined aluminium extrusions subjected to quasi-static and dynamic loading, has been investigated in order to compare the modelling approaches for situations close to industrial real life conditions. Both approaches could predict the sequence of adhesive failure observed in the experiments. The force-displacement curves of experiments and simulations were in fair agreement. The detailed solid element modelling approach performed slightly better than the simplified interface model; nevertheless, the good agreement of the simplified interface model was encouraging for industrial application. Both modelling approaches are considered being useful tools for numerical crashworthiness analysis of adhesive failure.

6. Future work

The potential existence of rate dependent fracture must be clarified in the future, which requires advanced dynamic strain measurement test methods. Furthermore, it would be interesting to perform another validation test for a different loading case involving not only a sequence of separated mode I (peeling) and mode II (shearing) failure, but also a combination of these failure modes.

7. Acknowledgements

The experimental analysis of the adhesively butt-joined tubes by Prof. Schlimmer and co-workers from Kassel University is acknowledged as well as the work by Prof. Pickett and co-workers at Cranfield University for the evaluation of the fracture toughness and joined extrusion tests. Furthermore, the authors acknowledge the work of the different partners of the FOSTA project "Methodenentwicklung zur Berechnung von höherfesten Stahlklebverbindungen des Fahrzeugbaus unter Crashbelastung" [10].

8. References

[1] (2006) Special: Audi TT. Zeitschrift Automobil Industrie, Germany: Vogel Auto Medien GmbH & Co. KG

[2 Technical data sheet of Betamate™ 1496: http://automotive.dow.com/materials/products/betamate/bmate96.htm

[3] von Mises R (1928) Mechanik der plastischen Formanderung von Kristallen. ZAMM 8:161-185

[4] Schlimmer M (1974) Fliessverhalten plastisch kompressibler Werkstoffe. Dissertation, Technische Hochschule Aachen

[5] Drucker, DC, Prager W 1952) Soil Mechanics and Plastic Analysis in Limit Design. Quarterly Applied Mathematics 10(2):157-165

[6] Mahnken R, Schlimmer M (2005) Simulation of strength difference in elasto-plasticity for adhesive materials. International Journal for Numerical Methods in Engineering 63(10):1461-1477

[7] Deshpande VS, Fleck NA (2000). Isotropic constitutive models for metallic foams. Journal of the Mechanics and Physics of Solids 48:1253-1283

[8] Johnson, GR, Cook, WH (1985) Fracture Characteristics of Three Metals Subjected to Various Strain, Strain Rates, Temperatures and Pressures. Engineering Fracture Mechanics 21(1):31-48

[9] Sato C, Ikegami K (1999) Strength of Adhesively-Bonded Butt Joints of Tubes Subjected to combined High-Rate Loads. Journal of Adhesion, 1999;70:57-73

[10] (2005-2007) Methodenentwicklung zur Berechnung von höherfesten Stahlklebverbindungen des Fahrzeugbaus unter Crashbelastung. FOSTA-Nr. P676

[11] Camanho PP, Davila CG, Ambur DR (2001) Numerical Simulation of Delamination Growth in Composite Materials. NASA Langley Research Center, Hampton Virginia, NASA TP-2001-211041

[12] Camanho PP, Matthews FL (1999) Delamination Onset Prediction in Mechanically Fastened Joints in Composite Laminates. Journal of Composite Materials 33:906-927

[13] Johnson AF, Pickett AK, Rozycki P (2001) Computational methods for predicting impact damage in composite structures. Composite Science and Technology 61(15):2183-2192

[14] Greve L, Pickett AK (2005) Delamination testing and modelling for composite crash simulation, Composite Science and Technology [in press, online available]

[15] ABAQUS User Manual, http://abaqus.com

[16] PAM-CRASH™ PAM-SAFE™ Version 2005 Manuals, Engineering System International, www.esi-group.com

[17] Hillerborg A, Modeer M, Petersson P E. (1976) Analysis of Crack Formation and Crack Growth in Concrete by Means of Fracture Mechanics and Finite Elements. Cement and Concrete Research 6:773-782

[18] Hahn O, Hennemann OD, Schlimmer M (2005-2007) Methodenentwicklung zur Berechnung und Auslegung geklebter Stahlbauteile für den Fahrzeugbau. FOSTA-Nr. P563/76 ZN

[19] Dilger K, Hahn O, Hennemann OD (2000-2002) Untersuchungen zum Crashverhalten geklebter und hybridgefügter Stahlblechverbindungen. FOSTA-Nr. P477

[20] Disse T. (2004) Untersuchungen zum geschwindigkeitsabhängigen Festigkeits- und Verformungsverhalten von Klebverbindungen. Dissertation, Universität Paderborn, Shaker Verlag
[21] ISO international Standard DIS15024. Fibre-reinforced plastic composites – Determination of Mode I inter-laminar fracture toughness, GIC, for unidirectionally reinforced materials.
[22] Steinbrecher G, Buchman A, Sidess A, Sherman D. (2006) Characterization of the mode I fracture energy of adhesive joints", International Journal of Adhesion and Adhesives [available online]
[23] Blackman BRK, Kinloch AJ, Paraschi M, Teo WS (2003) Measuring the mode I adhesive fracture energy, GIC, of structural adhesive joints: the results of an international round-robin. International Journal of Adhesion and Adhesives 23(4):293-305

9. Appendix

Denomination	Symbol	Value	Source	Model* S	Model* I
Elastic modulus	E	*1.82 GPa*	[18]	x	x
Shear modulus	G	*0.625 GPa*	[18]	x	x
Elastic Poisson's ratio	ν^e	*0.4*	[18]	x	-
Plastic Poisson's ratio	ν^p	*0.23*	[18]	x	-
Shape parameter of yield potential	α	*1.335*	-	x	-
Shift stress of yield surface	σ_0	*-0.026 GPa*	-	x	-
Shape parameter of flow potential function	β	*1.4*	-	x	-
Uniaxial quasi-static tensile yield strength	σ_T^{sta}	*0.032 GPa*	[18]	x	x
Uniaxial quasi-static compression yield strength	σ_C^{sta}	$1.6\,\sigma_T^{sta}$	[18], [20]	x	-
Uniaxial dynamic tensile yield strength	$\sigma_T\left(\dot{\varepsilon}_T^p \rightarrow 156 s^{-1}\right)$	$2\,\sigma_T^{sta}$	[20]	x	-
Strain rate model parameter	C	*0.36*	-	x	-
JC fracture curve parameters	d_1	*0.054*	-	x	-
	d_2	*0.356*	-	x	-
	d_3	*5.92*	-	x	-
Mode I critical strain energy release rate	G_{IC}	*5 kJ/m²*	-	-	x
Mode II critical strain energy release rate	G_{IIC}	*10 kJ/m²*	estim.	-	x
Mode I strength	$\sigma_I^{\max}$	*0.032 GPa*	-	-	x
Mode II strength	$\sigma_{II}^{\max}$	*0.034 GPa*	-	-	x

**) Model parameters required for solid element model (S), or interface model (I).*

Table 1. Collection of elastic, quasi-static/dynamic yield, fracture, and fracture toughness properties of the high strength adhesive Betamate™ 1496.